Available online at www.sciencedirect.com

SCIENCE DIRECT®

Remote Sensing of Environment 92 (2004) 447–464

Remote Sensing of Environment

www.elsevier.com/locate/rse

Upscaling ground observations of vegetation water content, canopy height, and leaf area index during SMEX02 using aircraft and Landsat imagery

M. C. Anderson[a,*], C. M. U. Neale[b], F. Li[c], J. M. Norman[a], W. P. Kustas[c], H. Jayanthi[b], J. Chavez[b]

[a]Department of Soil Science, University of Wisconsin-Madison, 1525 Observatory Drive, Madison, WI 53706, United States
[b]Department of Biological and Irrigation Engineering, Utah State University, Logan, UT 84322-4105, United States
[c]Hydrology and Remote Sensing Laboratory, USDA-ARS, Bldg. 007, BARC West, Beltsville, MD 20705, United States

Received 5 September 2003; received in revised form 1 March 2004; accepted 3 March 2004

Abstract

Microwave-based remote sensing algorithms for mapping soil moisture are sensitive to water contained in surface vegetation at moderate levels of canopy cover. Correction schemes require spatially distributed estimates of vegetation water content at scales comparable to that of the microwave sensor footprint (10^1 to 10^4 m). This study compares the relative utility of high-resolution (1.5 m) aircraft and coarser-resolution (30 m) Landsat imagery in upscaling an extensive set of ground-based measurements of canopy biophysical properties collected during the Soil Moisture Experiment of 2002 (SMEX02) within the Walnut Creek Watershed. The upscaling was accomplished using expolinear relationships developed between spectral vegetation indices and measurements of leaf area index, canopy height, and vegetation water content. Of the various indices examined, a Normalized Difference Water Index (NDWI), derived from near- and shortwave-infrared reflectances, was found to be least susceptible to saturation at high levels of leaf area index. With the aircraft data set, which did not include a short-wave infrared water absorption band, the Optimized Soil Adjusted Vegetation Index (OSAVI) yielded best correlations with observations and highest saturation levels. At the observation scale (10 m), LAI was retrieved from both NDWI and OSAVI imagery with an accuracy of 0.6, vegetation water content at 0.7 kg m^{-2}, and canopy height to within 0.2 m. Both indices were used to estimate field-scale mean canopy properties and variability for each of the intensive soil-moisture-sampling sites within the watershed study area. Results regarding scale invariance over the SMEX02 study area in transformations from band reflectance and vegetation indices to canopy biophysical properties are also presented.

Keywords: SMEX02; Landsat; Leaf area index

1. Introduction

The Soil Moisture Experiment of 2002 (SMEX02) was conducted to validate algorithms for retrieving soil moisture estimates from microwave remote sensing data acquired with aircraft and satellite-borne sensors. A specific focus in SMEX02 was to study the effects of spatially variable vegetation cover on soil moisture retrieval accuracy during periods of rapid vegetation growth. The presence of surface vegetation tends to obscure microwave emission from the soil, while enhancing the net flux with emission from water contained within the biomass (Jackson & Schmugge, 1991). While corrections based on vegetation water content can be applied (Jackson & O'Neill, 1990; Jackson & Schmugge, 1991), the soil moisture signature can become essentially undetectable at full canopy closure. Extensive ground-based sampling of biomass and water content was undertaken during SMEX02 to quantify the accuracy of retrieval correction techniques. For use in calibrating remote retrieval algorithms, these point measurements need to be upscaled to provide spatially continuous coverage over the study region at resolutions spanning the range in footprint of microwave sensors utilized in this experiment (500 m to 75 km). In

* Corresponding author. Tel.: +1 608 265 3288; fax: +1 608 265 2595.
E-mail address: mcanders@facstaff.wisc.edu (M.C. Anderson).

0034-4257/$ - see front matter © 2004 Elsevier Inc. All rights reserved.
doi:10.1016/j.rse.2004.03.019

addition, measures of spatial variability are required for analyzing retrieval sensitivity to expected errors in biomass specification.

A related Soil Moisture–Atmospheric Coupling Experiment (SMACEX; see, e.g., Kustas et al., this issue) ran concurrently with SMEX02 across the same study domain. A primary goal of SMACEX was to study the role of heterogeneity in soil moisture and vegetation cover in influencing land–atmosphere exchanges of energy, water, and carbon over a range of spatial scales. During the experiment, surface energy fluxes were measured continuously at 14 eddy-covariance towers distributed across the study area, and periodically along tracks flown by research aircraft. Spatially and temporally distributed information regarding crop height and leaf area are critical to SMACEX, as these canopy properties influence surface roughness, evaporation rates, and interpretation of remote sensing data.

Throughout the SMEX02/SMACEX experiment, intensive soil and vegetation measurements were collected in and around the Walnut Creek Watershed within a 6×30 km area just south of Ames, IA (Fig. 1), with less-intensive sampling in a 40×100 km area coincident with regional airborne sensor scan lines. This sampling scheme was structured to facilitate a multiple stage upscaling process. The sampling sites are well resolved in multiband aircraft imagery collected at 1.5-m resolution; correlations developed between spectral vegetation indices (VIs) and ground measurements can be used to produce maps of canopy biophysical properties across the watershed. Satellite-based radiometers, such as the Landsat 5 Thematic Mapper and Landsat 7 Enhanced Thematic Mapper+ (together referred to here as TM), have lower resolution (30 m for shortwave TM bands), but provide broader spatial coverage and can be used to aggregate to the scale of microwave footprint.

Of the many existing VIs, the Normalized Difference Vegetation Index (NDVI; Kriegler et al., 1969; Rouse et al., 1973): NDVI=(NIR−R)/(NIR+R), where R and NIR are reflectances in the red (~0.6 μm) and near-infrared (~0.8 μm) wavebands, respectively, has historically had the most usage in terms of remote vegetation mapping, but is susceptible to responses from the underlying soil under partial canopy cover. The family of soil-adjusted VIs of form (NIR−R)(1+L)/(NIR+R+L) include a factor L to compensate for the noise caused by the soil background (Huete, 1988). While the value of L was found to decrease with increasing vegetation cover, Huete suggested L=0.5 as an optimal value over the full range in cover. Numerical canopy reflectance simulations by Rondeaux et al. (1996) identified L=0.16 (the Optimized Soil Adjusted Vegetation Index; OSAVI) as minimizing soil-induced variability in VI, particularly for homogeneous canopies such as in grasslands and agricultural crops.

Vegetation indices based on NIR and red reflectances are problematic in that they tend to saturate at moderately high values of LAI (~2.5–3), where additional leaf area has a diminishing effect on canopy reflectance particularly in the red band (e.g., Carlson et al., 1990; Sellers, 1987). A related Normalized Difference Water Index (NDWI), computed from NIR and shortwave infrared (SWIR; ~1.2–2.5 μm) reflectances: NDWI=(NIR−SWIR)/(NIR+SWIR), has been

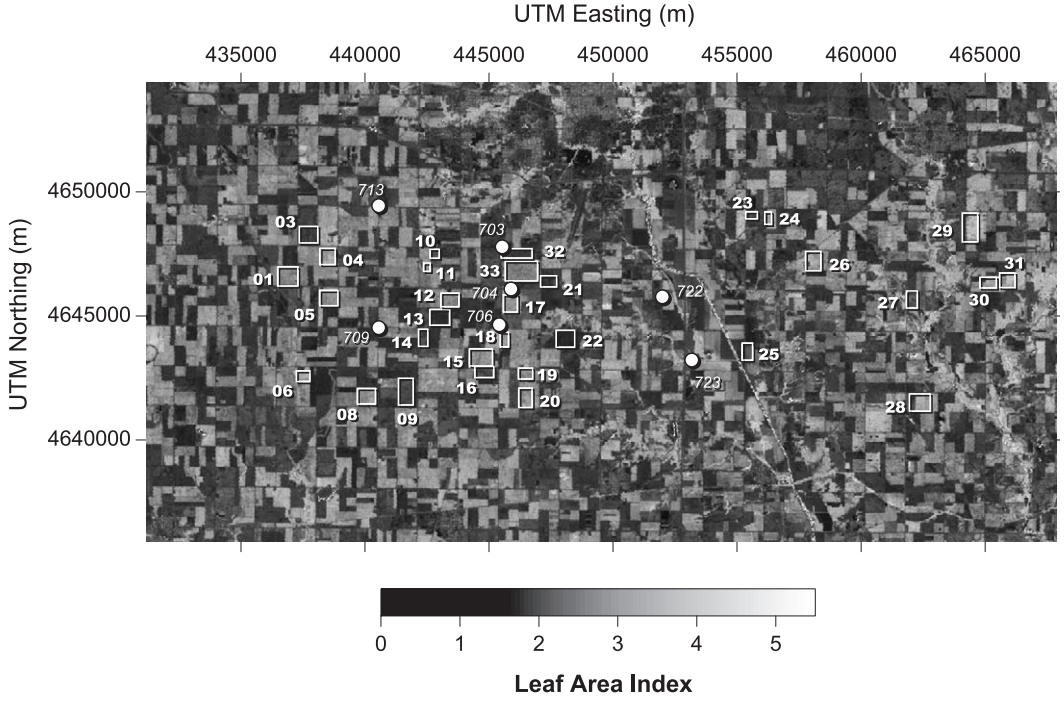

Fig. 1. Upscaled map of leaf area index over the Walnut Creek Watershed, derived from TM NDWI data for July 1, 2002. In general, the lower LAI fields on this date are soybean, while higher LAI fields are corn. Rectangles locate field-averaging boundaries used to aggregate biophysical properties to field scale at each sampling site; circles show positions of rain gauges referenced in Fig. 2.

found to be more sensitive than NDVI to leaf area and water content in closed canopies and saturates at higher LAI. Hardisky et al. (1983) found good correlation between canopy moisture and a form of NDWI (known as the Infrared Index; II) using a SWIR band replicating TM band 5 (1.55–1.75 μm). Gao (1996) recommended a shorter SWIR band at 1.24 μm, available on the Moderate Resolution Imaging Spectrometer (MODIS), which is more robust to atmospheric scattering.

The primary objectives of this paper are to (a) document vegetation conditions during SMEX02 that are relevant to microwave and land-surface modeling experiments, as reflected in the ground samples themselves; (b) use available aircraft and TM imagery to obtain robust estimates of field-scale mean canopy conditions and variability; and (c) form recommendations for upscaling to larger scales commensurate with microwave sensor footprints using remote sensing information. We focus on mapping canopy properties of leaf area index (LAI; leaf area/ground area), vegetation water content (θ_{veg}) and height (h_c); quantities that are integral to soil moisture retrieval and surface energy balance modeling. While the practical utility of empirical regressions between biophysical variables and vegetation indices in terms of remote retrieval is necessarily limited to the time and place over which the ground data are collected (Gobron et al., 1997; Verstraete et al., 1996), the extensive data set amassed during SMEX02 also provides more general information regarding the scaling of these relationships across agricultural landscapes.

2. Data

2.1. Ground observations

Within the Walnut Creek Watershed, 21 corn and 10 soybean fields were selected as sites for intensive soil moisture and vegetation sampling (Fig. 1). Vegetation data were collected within the watershed in four sampling rounds between June 15 and July 8: 12 field sites containing flux towers were sampled in each round, and the remaining 19 sites were sampled twice, in rounds 2 and 4 (Fig. 2 and Table 1). The full sampling interval encompassed the period from emergence to tasseling/full bloom in many area corn/soybean fields, and also included an extended 2-week drought (from 6/21 to 7/4), which had a significant impact on soil moisture and caused isolated regions of vegetation stress.

In each sampling round, multiple measurements of LAI, stand density, canopy height, plant phenology, ground cover percentage, and above-ground green and dry biomass were taken at each sampling site, with vegetation water content derived as the difference between green and dry biomass. Because canopy architecture can influence microwave scattering, plant biomass was separated into stem/stalk and leaf subcomponents. In addition, digital photographs were taken to provide a visual record of stand conditions at the time the samples were collected.

2.1.1. Vegetation sampling strategy

Three vegetation-sampling locations were identified in each of the 31 intensive watershed monitoring sites using high-resolution aerial imagery collected on June 16, 2002: one location with moderately high vegetation cover, one with low cover, and a third representing average cover. Field WC25 (shown in Fig. 3) was assigned an additional location characterizing conditions on a sandy hillslope in the northeast corner of the field, where crop growth was notably stunted. Sampling locations were selected such that soil and canopy conditions were fairly homogeneous in surrounding areas on scales of tens of meters, and where the vegetation appeared healthy and capable of surviving through the experiment. A large (1.5×1.5 m) white aerial target was installed at the corner of each sampling location to facilitate registration of ground samples with respect to the aircraft data. The coordinates of each target were recorded on the ground with a handheld Global Positioning System (GPS) unit, and each can be visually identified within the high-resolution aircraft imagery.

Each vegetation sampling location was 12-m long and 10 rows across. For statistical purposes, measurements were

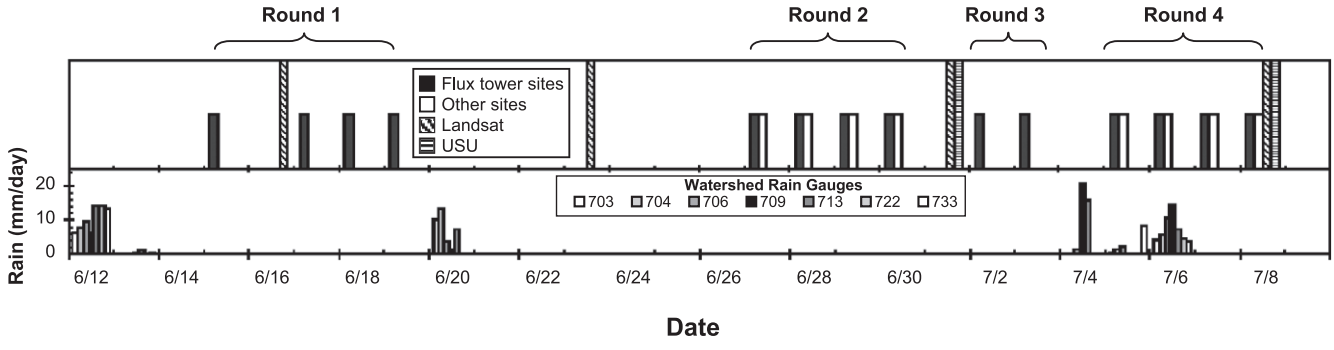

Fig. 2. Time sequence of vegetation sampling in the Walnut Creek Watershed during the SMEX02 campaign. Also shown are dates of USU aircraft and Landsat scenes used in this study. Lower panel shows daily precipitation measured at seven rain gauges in the watershed (see Fig. 1 for gauge locations).

Table 1
Vegetation sampling conducted at the SMEX02 watershed sites

Site	Crop[a]	Row spacing	Row direction	Round 1	Round 2	Round 3	Round 4
WC01	C	0.76	E–W		6/29		7/6
WC03[b]	S	0.38	N–S	6/18	6/28	7/2	7/5
WC04	C	0.76	E–W		6/30		7/8
WC05	C	0.76	N–S		6/28		7/5
WC06[b]	C	0.76	N–S	6/18	6/27	7/3	7/7
WC08	C	0.76	N–S		6/28		7/5
WC09	S	0.38	N–S		6/28		7/7
WC10[b]	S	flexcoil	n.a.[c]	6/18	6/29	7/2	7/7
WC11[b]	C	0.76	N–S	6/18	6/28	7/2	7/8
WC12	C	0.76	N–S		6/29		7/5
WC13[b]	S	0.76	E–W[d]; N–S[e]	6/18	6/28	7/2	7/8
WC14[b]	S	flexcoil	n.a.[c]	6/19	6/28	7/3	7/6
WC15[b]	C	0.76	E–W	6/17	6/28	7/2	7/8
WC16[b]	S	0.25[d]; 0.76[e]	E–W	6/17	6/29	7/2	7/8
WC17	C	0.76	E–W		6/27		7/6
WC18	C	0.76	N–S		6/27		7/6
WC19	C	0.76	E–W		6/28		7/5
WC20	C	0.76	E–W		6/28		7/5
WC21	S	0.38	E–W		6/27		7/7
WC22	S	0.38	N–S		6/29		7/7
WC23[b]	S	0.25	E–W	6/15	6/28	7/2	7/8
WC24[b]	C	0.76	N–S	6/15	6/28	7/2	7/8
WC25[b]	C	0.76	E–W	6/18	6/29	7/2	7/8
WC26	C	0.76	N–S		6/28		7/6
WC27	C	0.76	E–W		6/29		7/7
WC28	C	0.76	N–S		6/29		7/7
WC29	C	0.76	E–W		6/28		7/6
WC30	C	0.76	E–W		6/29		7/6
WC31	C	0.76	E–W		6/28		7/5
WC32	S	0.38	E–W		6/27	7/2	7/8
WC33[b]	C	0.76	E–W	6/18	6/27	7/3	7/7

[a] C=corn; S=soybean.
[b] Eddy correlation flux tower/s located on-site.
[c] Not applicable: in flexcoil soybean plantings, seeds are broadcast uniformly rather than in rows.
[d] Conditions at sampling locations 1 and 2.
[e] Conditions at sampling location 3.

taken in every second row yielding five sets of observations per location. In the first sampling round, vegetation samples were collected in the first 3-m segment closest to the aerial target; in the second round, from the second 3-m segment, etc. (see Fig. 3). For comparison with reflectance data, the five measurements made at each location were averaged to yield three data points per site per sampling round.

2.1.2. Vegetation height and stand density measurement

Average plant height in a 3-m segment in each sampling row was estimated using a meter stick. In corn, this nominal height estimate excluded the extreme tips of vertical leaves to better represent the scale of the effective surface roughness element.

In fields cultivated in rows, the areal stand density (ASD; plants/m^2) was determined by measuring the number of plants within a 1-m segment selected randomly along the sampling row (row density, RD; plants/m), and the row spacing (RS; m): ASD=RD/RS. Two of the soybean fields sampled (WC10 and WC14) were planted with a flexcoil system, where seeds are broadcast uniformly rather than in rows. For flexcoil plots, areal stand density was computed as ASD=AD×2, where AD is the number of plants counted within a wire frame with dimensions 1×0.5 m.

2.1.3. Vegetation water content measurement

Destructive above-ground biomass samples were collected from each sampling row, totaling five plants per location per sampling round. A plant of average height was cut at the ground surface, separated into stem and leaf components (except in the first sampling round, when soybean plants were too small for separation), and placed into two paper bags. The bags were oven dried to constant weight for 4–5 days at 110 °F.

The leaf, stem, and total water content (θ_{leaf}, θ_{stem}, θ_{plant}; g/plant) of each plant was computed as $\theta_{leaf}=(B'_g - B'_d)_{leaves}$, $\theta_{stem}=(B'_g - B'_d)_{stem}$, and $\theta_{plant}=\theta_{leaf}+\theta_{stem}$, where B'_g is the green biomass+bag weight of the component and B'_d is the dry biomass+bag weight. Tests showed that the change in B'_g during transport from field to laboratory was negligible in most cases. Areal vegetation water content (θ_{veg}; kg/m^2) is then given by $\theta_{veg}=10^{-3}\times\theta_{plant}\times$ASD.

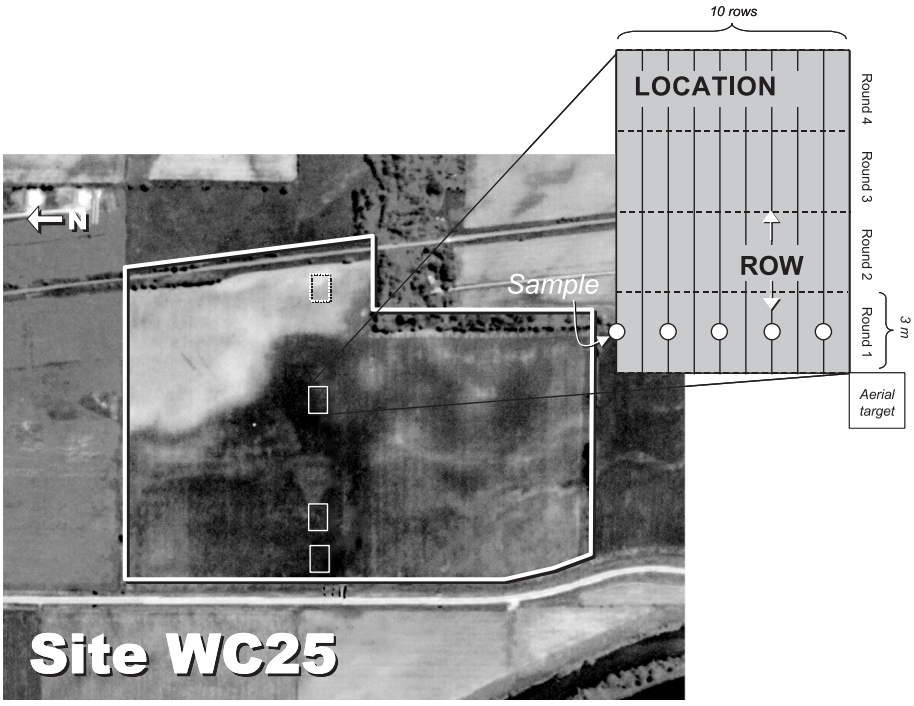

Fig. 3. Schematic diagram demonstrating the vegetation sampling strategy employed in SMEX02. WC25 was assigned an additional sampling location to characterize stunted crop conditions on a sandy hillslope in the northeast corner of the field.

2.1.4. Leaf area index measurement

Leaf area index was measured using a LAI-2000 (LI-COR, Lincoln, NE) Plant Canopy Analyzer, which compares above- and below-canopy light levels detected in five conical rings, with view zenith angle ranging from nadir to 75°, to infer LAI and characteristics of canopy architecture (Welles & Norman, 1991). The LAI-2000 units were programmed to average four observations into a single value, using one measurement taken above the canopy and four beneath the canopy: in the row, 1/4 of the way across the row, 1/2 of the way across the row, and 3/4 of the way across the row. This gives a good spatial average for row crops of partial cover. A mask blocking a 1/4 wedge of the sensor view was positioned to intercept direct solar radiation falling on the sensor surface.

The LAI-2000 is most optimally used under diffuse lighting conditions (overcast sky, or near dawn or dusk). Direct beam radiation reflecting off upper leaves in the canopy can cause these leaves to be indistinguishable from the background sky brightness, thus the sensing system tends to underestimate total leaf area (Welles & Norman, 1991). During SMEX02, however, resource and time constraints required that some data be collected midday during periods of sunshine. To estimate the magnitude of this effect, 100 measurements were made under both sunny and diffuse conditions in corn and soybean stands with LAI ranging from 0.2 to 3.3 and at solar zenith angles of 17–70°. On average, measurements made in sunny conditions were biased low by $10\pm1\%$ (0.14 units of LAI on average) with respect to diffuse measurements. All LAI measurements made in sunshine have therefore been increased by 10%.

2.1.5. Temporal and spatial variability in vegetation conditions during SMEX02

Fig. 4 shows the time-development of canopy height, LAI, and vegetation water content during SMEX02 in each of the 31 watershed sampling fields. The variability in canopy conditions near the end of the experiment is considerable, reflecting differences in soil type, planting dates, and cultivation practices. Note that site WC25 (corn) stands out as having a depressed growth pattern, particularly in terms of LAI and water content. Visual inspection showed the entire field lagging other corn-fields in the watershed in terms of crop development, possibly due to moisture stress related to high soil sand content.

Two trends in canopy structure may be of note for studies of microwave radiative transfer. While plant water content (θ_{plant}) was found to be very well correlated with green biomass (corn and soybean were 86% and 80% water on average, respectively, with R^2=0.997), the fractional water content (θ_{plant}/green biomass) decreased slowly with time at a rate of $-0.28\pm0.01\%$ day^{-1} on average for corn and $-0.31\pm0.02\%$ day^{-1} for soybean (see Table 2). While this may be due in part to phenological changes, with the plant investing more resources to dry mass and architectural stability as its

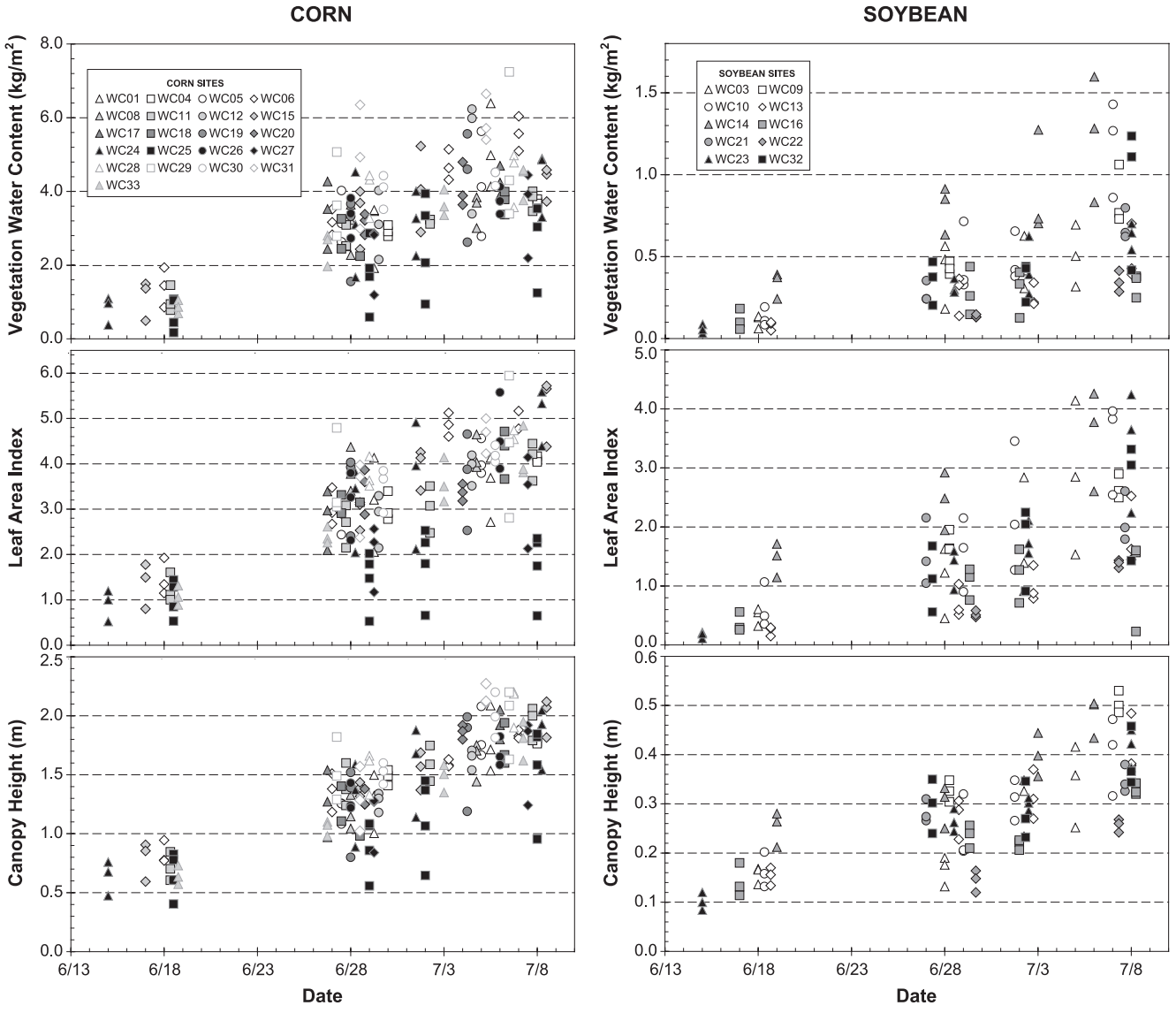

Fig. 4. Temporal variation in sampling location-averaged measurements (three per site) of vegetation water content, LAI, and canopy height.

height increases, some extreme cases may be partially stress induced. The allocation of above-ground biomass between leaves and stems also varied through the experiment. The fraction of total above-ground dry biomass contained in leaves decreased at a rate of $-1.04\pm0.04\%$ day^{-1} in corn and $-1.33\pm0.10\%$ day^{-1} in soybean, while the leaf to total water content ratio decreased by $-0.52\pm0.03\%$ day^{-1} in corn and $-0.84\pm0.07\%$ day^{-1} in soybean. Shifts in allocation of biomass from leaves to stems occur in response to increased demands for structural stability, saturation in leaf light-gathering capacity, and translocation of materials for grain/pod production.

Among the canopy properties emphasized here, θ_{veg} and canopy height are both correlated with leaf area index (R^2~0.7), with different functional relationships for corn and soybean (Fig. 5). Vegetation water content is linearly related to LAI, while canopy height is better fit with a power law, indicating a very early stage of rapid vertical growth with little change in leaf area. The structural differences between corn and soybean evident in Fig. 5 are further manifested in relationships derived with spectral vegetation indices (below).

2.1.6. Interpolation to remote imaging dates

To provide best estimates of canopy conditions at the times of remote sensing image acquisition (Fig. 2), the row-averaged ground data at each sampling location were interpolated (or extrapolated) linearly in time between sampling rounds. Given the relatively short sampling interval (~5–10 days) and the small number of sampling events per site (2–4), a piece-wise linear fit was deemed

Table 2
Rate of change (Δ) in three biophysical ratios measured in corn and soybean during SMEX02[a]

Ratio	Crop[b]	N[c]	Δ (% day^{-1})	σ_Δ (% day^{-1})	RMSD (%)	Value (6/27) (%)
θ_{plant}/B_g	C	826	−0.28	0.01	1.58	88.03
	S	479	−0.31	0.02	2.67	82.51
$B_{d,leaf}/B_d$	C	826	−1.04	0.04	7.81	55.11
	S	404	−1.33	0.10	7.70	68.59
$\theta_{leaf}/\theta_{plant}$	C	826	−0.52	0.03	5.60	36.54
	S	404	−0.84	0.07	5.29	54.06

[a] Here θ_{leaf} and θ_{plant} are leaf and plant water contents, B_d and B_g are dry and green plant biomass, and $B_{d,leaf}$ is leaf dry biomass. Additionally, N is the number of samples, Δ is the rate of change in the ratio determined by linear regression with respect to sampling day, σ_Δ is the standard error in the rate, and RMSD is the root mean square of the regression residuals. Also included is the regression estimated ratio for June 27.

[b] C=corn ; S=soybean.

[c] All plant samples were used in the regression. Only whole plant biomass and water content was measured in soybean during the first sampling round (before June 27).

adequate and better justified than nonlinear curve fitting. Sampling data at a given site have been included in the analysis only if the imaging date was bracketed by sampling events (interpolation), or if the site was sampled within 2 days of the imaging date (extrapolation).

2.2. Remote sensing observations

2.2.1. Aircraft reflectance data

Throughout SMEX02, high spatial resolution visible, NIR and thermal imagery were collected periodically over

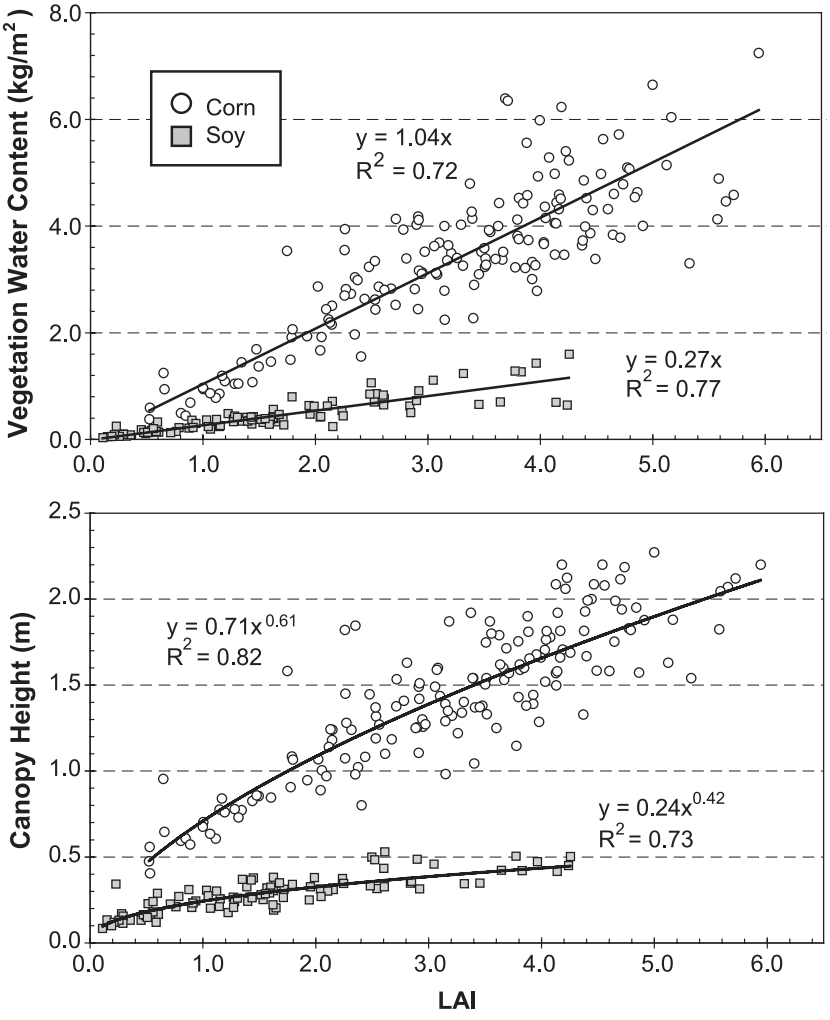

Fig. 5. Comparison of vegetation water content and canopy height measurements with LAI observed in corn and soybean during SMEX02, overlaid with linear (water content) and power law (canopy height) fits.

the Walnut Creek Watershed with the Utah State University (USU) airborne digital imaging system (Cai & Neale, 1999; Neale & Crowther, 1994), mounted in the belly of a twin engine Piper Seneca II aircraft. The data used in this study were acquired on 6/16, 7/1, and 7/8 at an altitude of 3200 m above ground level, resulting in a nominal pixel resolution of 1.5×1.5 m in the shortwave bands and a swath width of 3044 m. The shortwave component of the system consists of three Kodak Megaplus 4.2i digital cameras, with EPIX grabbing boards recording images in binary format. Each camera contains an 18.5×18.5 mm CCD chip having 2029(H) X 2044(V) light sensitive pixels. Interference filters were used to record the canopy responses in the green (0.545–0.560 μm), red (0.665–0.680 μm), and NIR (0.795–0.809 μm) wavebands, respectively (Table 3). An onboard GPS was used to navigate along pre-planned flight lines over the watershed, and to geo-reference the digital imagery. On days of Landsat satellite overpasses, the entire study region was imaged at high resolution such that the acquisition time bracketed the Landsat overpass time.

Calibrated visible/NIR imagery was obtained using incoming irradiance data measured with an Exotech radiometer with TM bands 1–4 placed over a leveled standard barium sulfate reflectance panel with known bidirectional reflectance properties. The radiometer was sampled every minute throughout the duration of the flight. Outgoing radiation was obtained with the system calibration equations using the same radiometer. The calibration was conducted in a separate experiment, relating image digital numbers with radiometer radiance in the corresponding waveband for different shutter speeds.

Finally, visible and near-infrared reflectances were extracted from the calibrated imagery in areas coincident with the 94 ground sampling locations. The associated aerial target was located in the imagery, and a 10 row×10 m subarea approximating each sampling location was selected at the appropriate orientation with respect to the target. Band reflectances were linearly averaged over these subareas. A final calibration check with respect to Landsat was then applied (see Section 2.2.2).

Table 3
Remote sensing imaging bands available with the USU aircraft and Landsat 5 (L5) TM and Landsat 7 (L7) ETM+ instruments

	USU		#	Landsat	
	Band (μm)	Resolution[a] (m)		Band (μm)	Resolution (m)
Blue			1	0.45–0.52	30
Green	0.545–0.560	1.5	2	0.52–0.60	30
Red	0.665–0.680	1.5	3	0.63–0.69	30
NIR	0.795–0.809	1.5	4	0.76–0.90	30
SWIR			5	1.55–1.75	30
SWIR			7	2.08–2.35	30
Thermal	10.5–12.5	6	6	10.40–12.50	120 (L5); 60 (L7)

[a] Effective spatial resolution at 3200-m altitude.

2.2.2. Landsat reflectance data

During the time the USU aircraft was in Iowa, Landsat scenes with minimal cloud cover over the watershed were acquired on 6/23 (Landsat 5), and 7/1 and 7/8 (Landsat 7). The original level 1G TM data were geo-registered with respect to road intersections, then atmospherically corrected with the MODTRAN radiative transfer model (Berk et al., 1998) using radiosonde data and default aerosol profiles. These atmospheric corrections were compared with results obtained using the Simulation of the Satellite Signal in the Solar Spectrum (6S; Vermote et al., 1997) software package and found to be consistent (Jackson et al., 2004). Details regarding the TM calibration process are described by Jackson et al. (2004) and Li et al. (2004).

Because the aerial targets could not be resolved in the 30-m Landsat imagery, reflectances at ground-sampling locations were extracted by selecting the pixel closest to the recorded GPS coordinate, or by averaging two adjacent pixels when the target lay on a pixel boundary.

Imagery from both Landsat and the USU aircraft were concurrently available on 7/1 and 7/8. Statistical comparisons between calibrated reflectances in the green, red, and NIR bands at the sampling locations showed residual biases (aircraft-TM) of 0.039, 0.015, 0.001, respectively, due to uncorrected atmospheric effects in the airborne imagery. To improve comparability between data sets, the USU reflectances were offset by these amounts.

2.2.3. Landcover classification

A supervised classification was conducted by Doraiswamy et al. (2004) using a 12-band image set covering the regional SMEX02 domain, consisting of bands 3,4,5, and 7 extracted from Landsat images acquired on May 14, July 1, and July 17, 2002. The overall classification accuracy was 95% in comparison with ground truth data collected in June and July. Within the Walnut Creek Watershed domain (Fig. 1), corn and soybean occupied 86% of the total area, with an additional 7% in roads, 4% grass, 2% trees, and trace proportions of pixels classified as urban and alfalfa. Of the total area covered by corn and soybean, corn comprised 48% of the pixels and soybean, 52%.

3. Development of retrieval relationships

Again, a primary objective of this study is to develop functional relationships between remotely sensed vegetation indices and ground observations of canopy biophysical properties that can be used to obtain robust spatial averages and measures of variability over a range in scales. Scales of interest include the “observation scale”, the area represented by ground measurements acquired during SMEX02 (~10×10 m); the “field scale”, nominal patches in the landscape over which conditions are relatively homogeneous (~500×500 m on average over the watershed); and the scale of the microwave sensor footprint (up to 75 km).

At each ground sampling location in the watershed study area, vegetation indices were computed from collocated aircraft red and NIR and TM band 3, 4, and 5 reflectances obtained as described in Section 2.2. NDVI and OSAVI indices were generated from both data sets, while the inclusion of the SWIR band 5 in the TM sensor additionally allowed computation of the water-sensitive NDWI index. Fig. 6 shows the relationships between the OSAVI and NDWI indices and time-interpolated measurements of LAI, θ_{veg}, and canopy height. Of the indices studied, NDWI showed the greatest sensitivity to biophysical properties at high LAI. If a saturation threshold is defined where a given VI, averaged within LAI bins of width 0.5, reaches 95% of the full range in binned VI, then NDVI saturates at LAI ≈ 3.5, OSAVI at LAI ≈ 4.0, and NDWI at LAI ≈ 4.5.

From a temporal standpoint, Fig. 7 indicates that indices computed from red and NIR reflectances at the 94 sampling

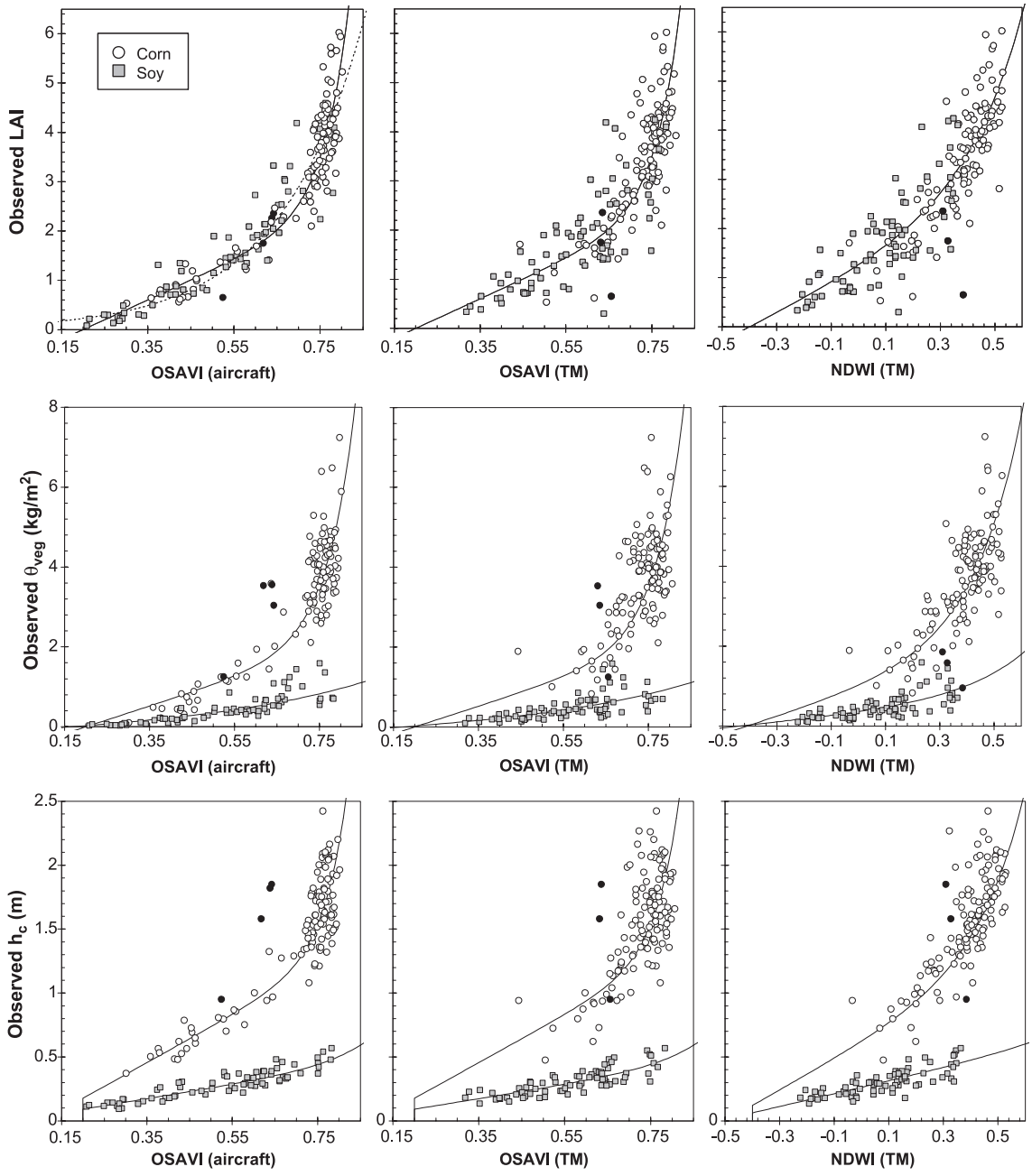

Fig. 6. Comparison of measurements of LAI (top row), vegetation water content (middle row), and canopy height (bottom row) with vegetation indices extracted from USU aircraft and TM imagery. Solid lines represent expolinear fits of the form in Eq. (1) (coefficients listed in Table 4); fits derived with respect to the aircraft OSAVI indices (left column) are also plotted on the TM OSAVI distributions (middle column). For comparison, the dotted line in the upper leftmost panel shows a pure exponential fit to LAI vs. $OSAVI_{USU}$. Solid circles indicate data collected at WC25 during the fourth sampling round, which were excluded from all regressions.

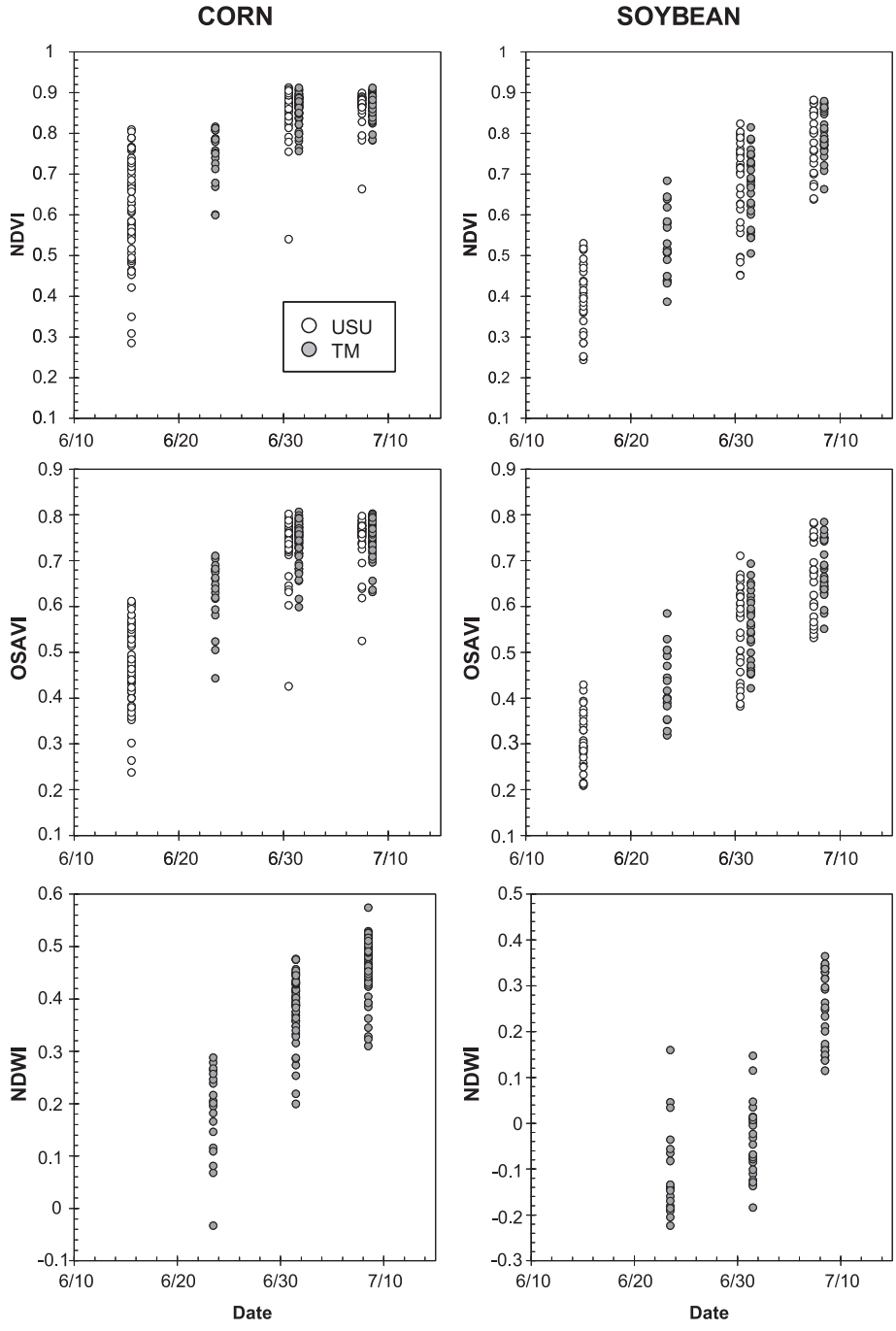

Fig. 7. Temporal variation in NDVI, OSAVI, and NDWI vegetation indices computed from USU aircraft and Landsat reflectances at corn and soybean sampling locations during SMEX02.

locations began to saturate in corn between July 1 and 8, while the LAI measured at most sites continued to increase (Fig. 4). During this week, cornfields in the watershed began tasseling, while soybean entered full bloom. Other studies have noted a saturation or downturn in NDVI at tasseling, attributed to concomitant changes in chlorophyll absorption resulting in increased reflectance in the visible wavelengths (Gitelson et al., 2003; Vogelmann & DeFelice, 2003). Using a hand-held radiometer, Tucker et al. (1979) observed maximum NDVI in corn occurring between the 12-leaf stage and first tassel. In soybean, the turnover did not occur until the appearance of first pod; only a small change in slope was observed at full bloom. This is consistent with results in Fig. 7 showing that indices over soybean did not saturate during SMEX02, although LAIs approaching 4.0 were attained (Fig. 4). The NDWI index did not saturate over either crop.

As evidenced in Fig. 6, the TM VIs show consistently greater scatter with respect to ground observations than do the aircraft derived indices. Before canopy closure, significant

subfield heterogeneity existed at scales exceeding ~10 m due to variable soils, slopes, and weed densities. While the individual sampling locations were well resolved at the meter scale, the 30-m TM data are affected to some extent by subpixel heterogeneity, weakening the correlation with VI. Note that data collected at WC25 during the 4th sampling round (highlighted in Fig. 6) are outliers from the general distributions, indicating unusual growing conditions (stress) or atypical reflectance contributions from the sandy background soil.

Of the total set of reflectance vs. biophysical variable data points plotted in Fig. 6, 65% were randomly selected and used to fit functions of the form

$$y = (a \times VI + b) \times (1 + c \times \exp[d \times VI]) \quad (1)$$

where y is LAI, θ_{veg}, or canopy height, and VI is OSAVI derived from the aircraft data set ($OSAVI_{USU}$) or NDWI from the Landsat reflectances ($NDWI_{TM}$); the resulting regression coefficients are listed in Table 4. Data collected during the 4th sampling round at WC25 have been omitted from the regressions, as these data are recognized as outliers and served to corrupt the general trends. As evident in Fig. 6 and also noted by Thenkabail et al. (1994), the relationships between LAI and the VIs tested are similar for corn and soybean, while θ_{veg} and h_c require crop-specific functionals. Given the significant structural differences between corn and soybean canopies (Fig. 5), this is not surprising. Regressions developed against the aircraft OSAVI data translate well to the TM OSAVI distributions, despite the larger scatter (Fig. 6).

One functional advantage to the expolinear regression form given in Eq. (1) is that the linear section (at low VI) extrapolates to bare soil conditions (i.e., LAI=θ_{veg}=h_c=0) at reasonable values of VI. Each fit in Fig. 6 has been forced through zero (bare soil) at the same value of VI (at OSAVI=0.2, and NDWI=−0.4) to provide consistency between retrieved biophysical properties. The selection of these bare-soil limits was driven primarily by the distributions of LAI and θ_{veg} vs. VI among the soybean sites, which had very low values during the first sampling round. In contrast, the canopy-height data approach some small but non-zero value at these VI limits. This is consistent with the height vs. LAI comparisons in Fig. 5, which show that height increases nonlinearly with respect to leaf area at very early stages. For ease of computation, this physiological phenomenon is accommodated by a step function at the zero-canopy threshold in VI (Fig. 6).

Statistical measures of retrieval performance, including the root-mean-square deviation (RMSD), mean bias error (MBE), and the coefficient of determination (R^2) between modeled and measured values, were computed using the remaining 35% of the data points, which were not utilized in the regressions and therefore constitute an independent validation set. These statistics are listed in Table 4, with graphical comparisons of observed vs. modeled values given in Fig. 8: the accuracy of LAI retrieval as measured by the RMSD was 0.6, vegetation water content −0.7 kg m^{-2}, and canopy height −0.2 m, with fractional errors on the order of 15–20%. At the observation scale, the higher-resolution $OSAVI_{USU}$ data predicted LAI with better skill, but was comparable in accuracy to $NDWI_{TM}$ in retrieving θ_{veg} and h_c. Retrievals based on $OSAVI_{TM}$ data were consistently poorer than $NDWI_{TM}$ retrievals (Table 4), primarily due to the lower saturation limits associated with the OSAVI. We can therefore surmise that if the SWIR band had been sampled from the aircraft platform, $NDWI_{USU}$ would be the preferable retrieval base in this setting, especially under full-canopy conditions.

Table 4
Statistical performance of canopy property retrievals using regression equations of the form $y=(a\times VI+b)(1+c\times\exp[d\times VI])$[a]

y	VI	Regression coefficients					Comparison with observations					
		Crop[b]	a	b	c	d	N	$\bar{O}$	RMSD	MBE	R^2	% Error
LAI	$OSAVI_{USU}$	B	4.00	−0.80	4.73e−6	15.64	60	2.59	0.58	−0.09	0.85	14.9
	$OSAVI_{TM}$		*Using USU regression*				69	2.62	0.84	−0.12	0.64	21.4
	$NDWI_{TM}$	B	2.88	1.14	1.04e−1	4.10	69	2.62	0.66	−0.02	0.76	17.8
θ_{veg} (kg m^{-2})	$OSAVI_{USU}$	C	3.45	−0.69	3.25e−5	13.57	64	2.44	0.67	−0.06	0.87	19.0
		S	0.58	−0.10	2.69e−1	2.31						
	$OSAVI_{TM}$		*Using USU regressions*				74	2.55	0.90	−0.18	0.76	24.5
	$NDWI_{TM}$	C	2.20	0.90	1.40e−1	4.80	74	2.55	0.66	−0.07	0.87	18.3
		S	0.70	0.31	1.76e−1	3.52						
h_c (m)	$OSAVI_{USU}$	C	1.86	−0.20	4.82e−7	17.69	64	1.08	0.18	−0.00	0.93	11.9
		S	0.55	−0.02	9.98e−5	9.52						
	$OSAVI_{USU}$		*Using USU regressions*				74	1.10	0.27	−0.03	0.84	16.9
	$NDWI_{TM}$	C	1.20	0.60	4.00e−2	5.30	74	1.10	0.20	−0.06	0.92	12.3
		S	0.50	0.26	5.00e−3	4.50						

[a] Here, N is the number of observations, $\bar{O}$ is the mean observed value, RMSD is the root-mean-square difference between the modeled (P) and observed (O) quantities, MBE is the mean-bias-error ($\bar{P}-\bar{O}$), R^2 is the coefficient of determination, and the percent error is defined as the mean-absolute-difference between P and O divided by the mean observed flux.

[b] C=corn; S=soybean; B=both corn and soybean.

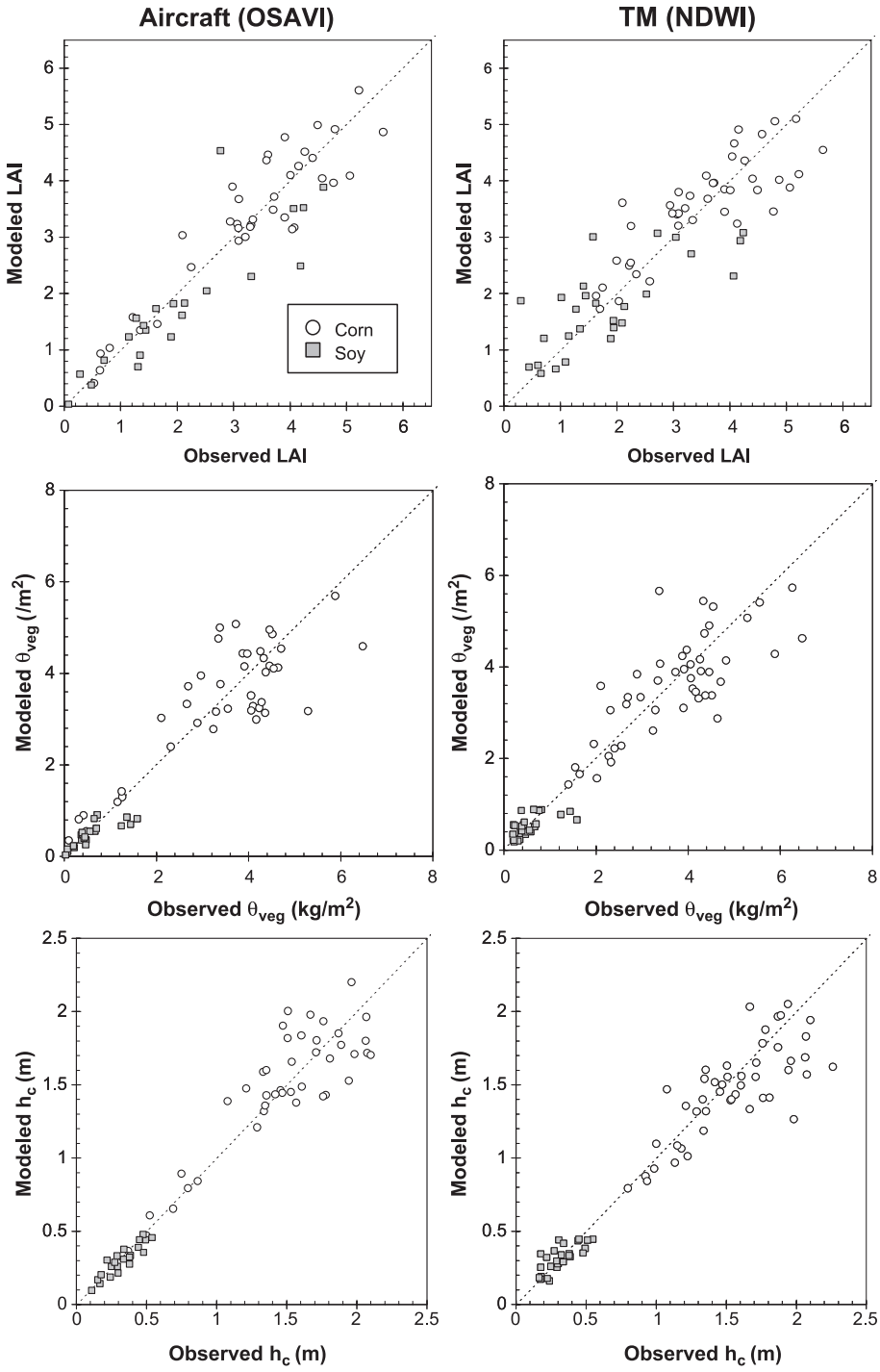

Fig. 8. Comparison of measured LAI, vegetation water content, and canopy height with modeled values retrieved from $OSAVI_{USU}$ (left) and $NDWI_{TM}$ (right) imagery at the observation scale (~10 m). These data points represent 35% of the total collected, and were not used in developing the regression equations used in the retrievals.

4. Upscaling canopy biophysical properties

While many techniques of varying complexity have been developed for spatially aggregating data on regular grids (see, e.g., Quattrochi & Goodchild, 1997), here we use simple linear averaging within nonoverlapping windows. For a transformation $y=g(x)$, an aggregated value of y ($\langle y\rangle$) can be obtained by: (A) computing y using the full resolution x, then aggregating y ($\langle y\rangle=\langle g(x)\rangle$); or (B) aggregating x, then applying the transformation g ($\langle y\rangle=g(\langle x\rangle)$). If the two methods agree over the operational range in spatial scales, the transformation is effectively scale invariant. While the transformation from radiance (x) to NDVI (y) is not strictly scale-invariant, biases between

methods A and B are generally minor for vegetated landsurfaces (e.g., De Cola, 1997; Friedl et al., 1995; Hall et al., 1992). The same is not necessarily true for the transformation from VI (x) to biophysical property (y). The agreement between methods A and B will depend on the nonlinearity of the transformation function, g, and the level of subcoarse-pixel heterogeneity in x with respect to this nonlinearity, which will be scale- and scene-dependent.

4.1. Field-scale mean properties and variability

To obtain best estimates of field-scale vegetation conditions and in-field variability during SMEX02, aggregation method A was employed at each watershed soil-moisture-sampling site over large rectangular regions defined to lie within field boundaries, excluding roads, farmhouses, lawns, etc. (see Fig. 1). Using landcover classification information, crop-appropriate regression equations (Table 4) were applied to the 1.5-m aircraft OSAVI and 30-m Landsat NDWI data, yielding gridded maps of LAI, θ_{veg}, and h_c at corresponding resolutions. Unrestricted, the steep exponential fit at high VI can potentially generate absurdly high values at isolated pixels; thus, retrieved values were limited to the range observed (and expected) during SMEX02: LAI was capped at 6.0, θ_{veg} at 8 kg m^{-2}, and h_c at 2.5 m. These maps were then aggregated within each site boundary; field-scale averages and standard deviations for the four imaging dates are tabulated in Table A1 in Appendix A. While results from both TM VIs are statistically similar for June 23, the standard deviations in the $OSAVI_{TM}$ retrievals for the July dates are typically 50% higher than those from $NDWI_{TM}$ due to the steepness of the retrieval function at full canopy cover. At these later dates, NDWI provides a more conservative estimate of spatial variability.

The remotely upscaled values listed in Table A1 contain better information regarding mean field properties than do the ground samples themselves. For example, in field WC16 on July 8, upscaling gives field-scale LAI values of 2.9–3.2 for aircraft and TM retrievals while the ground-sample average is 1.6 (excluding location 3, which had atypically wide row spacing; Table 1). In this case, each of the sampling locations was sited in areas that ultimately produced relatively low yield, thus ground-sample averages underestimate the true mean field conditions. The remote sensing data provide a means for spatially weighting in-field variability, making unrepresentative sampling sites less problematic as long as a wide range in conditions are measured overall.

Fig. 9 displays a time series of LAI maps for sites WC15 and WC16, retrieved from the $OSAVI_{USU}$ and $NDWI_{TM}$ imagery. These fields are of particular importance to the SMACEX experiment, as a volume-imaging lidar system was sited at the interface between these fields to collect observations of atmospheric turbulence and evaporative fluxes over corn and soybean canopies (Eichinger et al., 2003). Additionally, two eddy correlation stations were deployed in each field. The aircraft imagery reveals small-scale structure in canopy cover in both fields, primarily reflecting varying soil conditions and topographic relief. Islands of dense weeds in WC16, apparent in the June imagery, have been eradicated with herbicide by 1 July leaving holes in the developing soybean canopy. The imprint of a decommissioned railroad line runs across WC15, reflecting local disturbances in soil texture and bulk density. This type of detailed spatial information will be critical to interpreting lidar results and in determining fetch conditions influencing eddy correlation data.

The June 16 and 23 maps reflect the rapid crop growth observed in the watershed over this interval. Between July 1 and 8, however, the aircraft VIs are predicting a small decrease in mean LAI in WC15 (corn) contrary to both observations and TM predictions, which indicate continued growth. This is presumably an artifact of saturation and downturn in the OSAVI index associated with tasseling in corn; field notes indicate that tasseling was initiated in WC15 in the week before July 8. Note that the OSAVI-derived LAI for WC16 (soybean) has not yet reached saturation by July 8 although the canopy was at full bloom, in agreement with spectral-phenological behavior observed by Tucker et al. (1979). In this case, saturation effects in the $OSAVI_{USU}$ fields may be exacerbated by the narrow bandwidth of the aircraft sensors.

4.2. Scale dependence of retrieval relationships

To assess the effect of the resolution of the remote sensing information used in the retrieval of canopy properties over the SMEX02 study area, aggregation methods A and B were used to upscale transformations from TM (NIR and SWIR) reflectances to NDWI, and from NDWI to biophysical properties. TM reflectance and NDWI data were aggregated from 30 m to 100 m, 200 m, 500 m, 1 km, and 5 km scales, simulating response to lower resolution sensors (the SWIR band on MODIS, for example, has 500-m resolution). These experiments demonstrate that while NDWI is effectively scale invariant over these scales in the Walnut Creek watershed, retrieval of LAI, θ_{veg} and h_c from remote sensing data at resolutions coarser than field-scale will impose a negative bias in the upscaled quantities (Fig. 10).

Given the almost even distribution of land-use in the Walnut Creek watershed between corn and soybean, the upscaling process can be approximated as $\langle y\rangle=\langle g_i(x_i)\rangle$ (aggregation method A) where i indicates the landcover class of each high-resolution pixel, assumed to be pure at the 30-m scale; or as $\langle y\rangle=f_c g_c(\langle x\rangle)+f_s g_s(\langle x\rangle)$ (method B), where f indicates the fraction of the coarse-scale pixel populated by corn (subscript 'c') or soybean ('s').

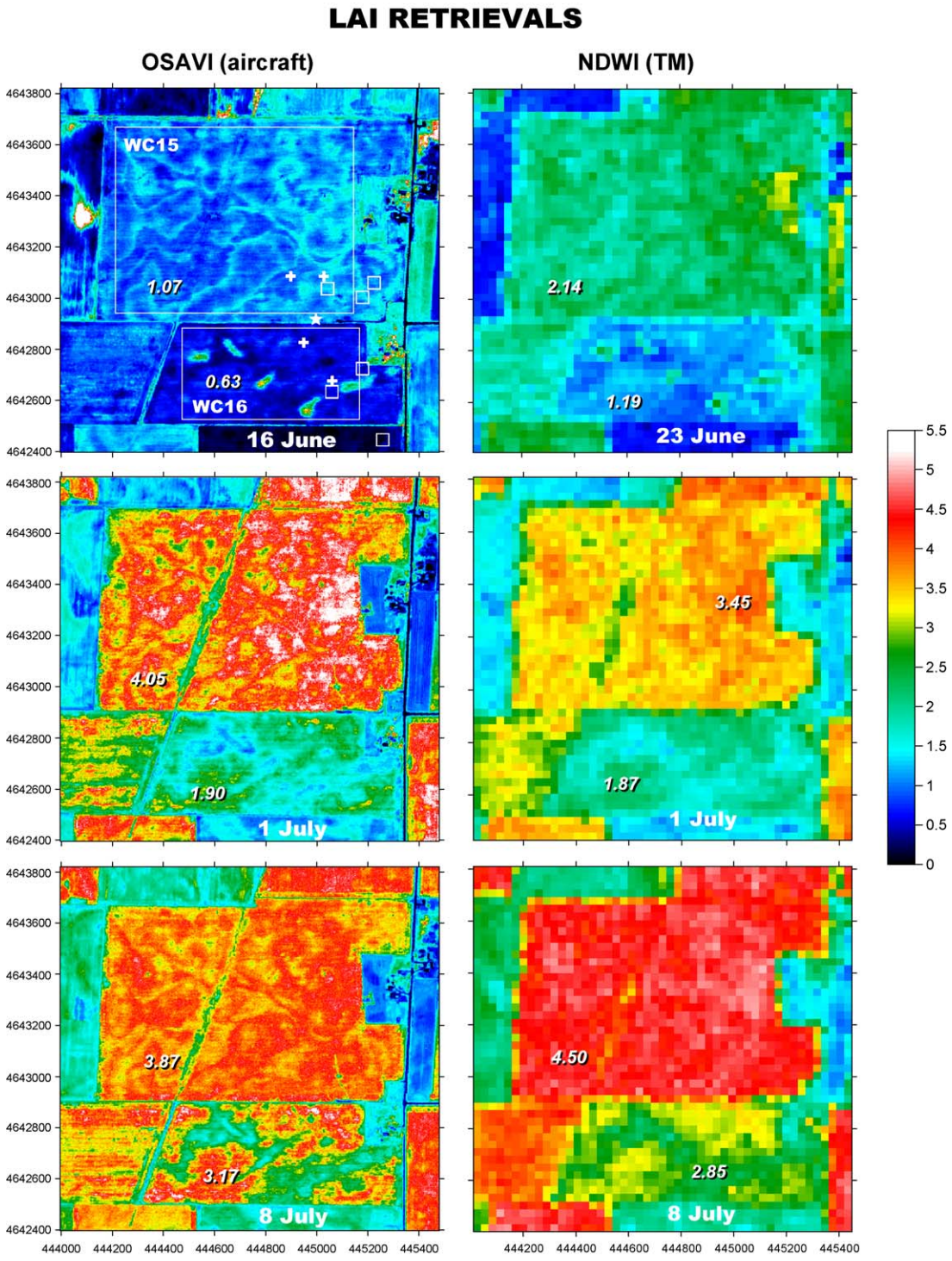

Fig. 9. Time series of LAI maps over sites WC15 and WC16, derived from $OSAVI_{USU}$ (left) and $NDWI_{TM}$ (right) images. Numbers in italics represent the field-average retrieved LAI. Large squares in first panel specify averaging boundaries, small squares show sampling locations (not to scale), crosses indicate flux towers, and the star indicates the position of the imaging lidar.

Here, pixels not classified as corn or soybean (~15% of the scene) have been excluded from the aggregation.

At the 100–200-m scale, and selecting only coarse-scale pixels that are pure corn or soybean (no mixtures), these two methods for aggregating biophysical properties agreed with an R^2 exceeding 0.99 and negligible bias. This suggests that the aggregation process, in this case, is independent of the scale of the VI data up to the field scale. Despite the in-field heterogeneity endemic to this landscape, it appears that the bulk of the conditions within a given field were confined to near-linear segments of the expolinear regression functions in Fig. 6.

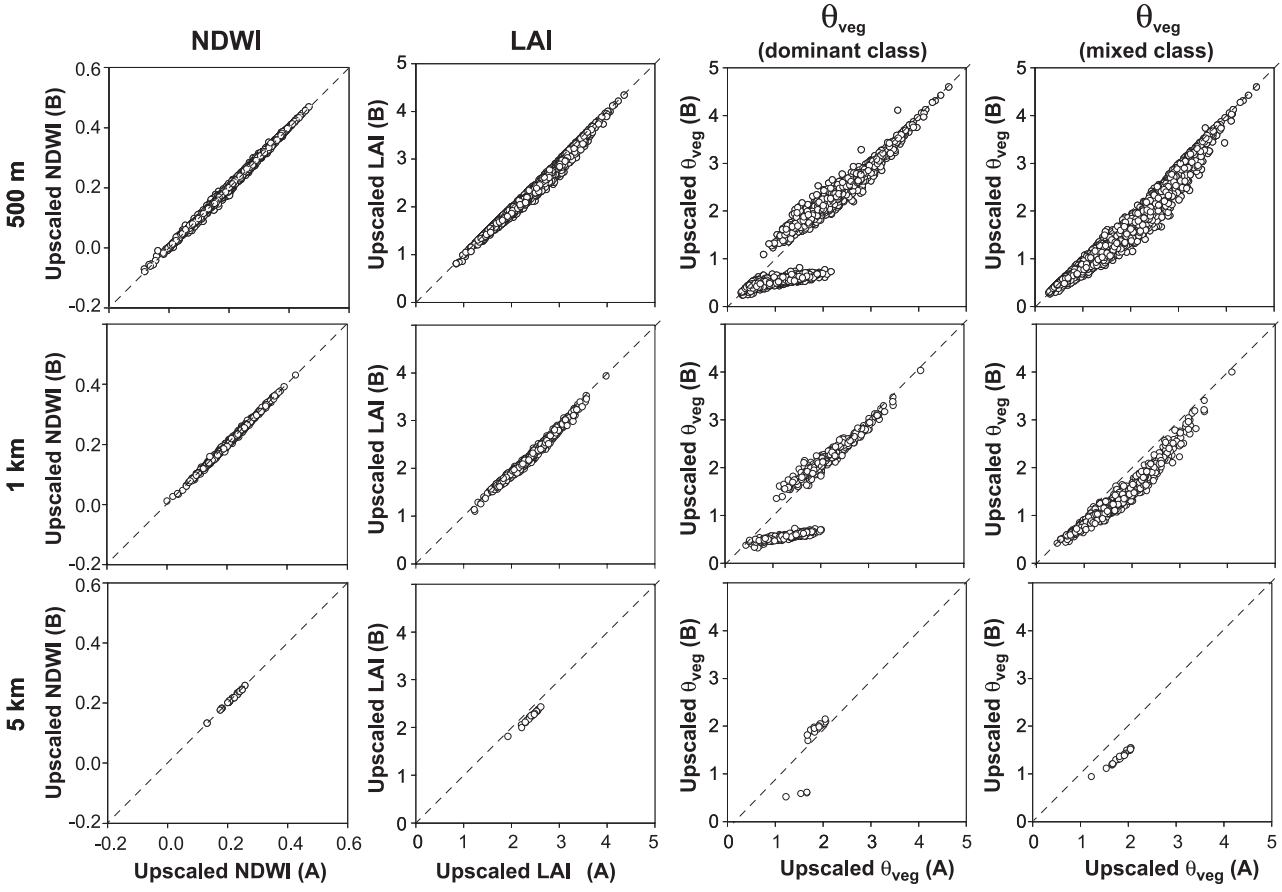

Fig. 10. Scale dependence of transformations from reflectance to NDWI (first column) and from NDWI to biophysical properties of LAI and vegetation water content (remaining columns). Aggregation methods A and B (described in text) are compared in upscaling from the 30-m native resolution of the TM-NIR and SWIR sensors to scales of 500 m (top row), 1 km (middle row), and 5 km (bottom row). Two aggregation scenarios are presented for θ_{veg}; one using only information about the dominant class in each coarse-resolution cell ("dominant class"), and a second assuming subpixel corn/soybean cropping fraction data are available ("mixed class").

At sensor resolutions coarser than the nominal field-scale, however, it is clear that subpixel mixing of different crop types will begin to affect the upscaling process, particularly for θ_{veg} and h_c, which have crop-dependent functional relationships with VI (Fig. 6). Over this landscape, LAI remains effectively scale invariant because corn and soybeans can be adequately described with a single function. The positive curvature in the retrieval function causes a small negative bias (−0.17 units of LAI at the 5-km scale) in values aggregated through method B (Fig. 10).

Given only information regarding the dominant cover type within a mixed coarse-scale cell (i.e., either f_c=1 or f_s=1), vegetation water content retrievals can be significantly degraded ("dominant class" panels shown in Fig. 10). Retrievals of canopy height (not shown) are similarly affected. In this case, pixels that contain slightly more than half soybean and therefore assigned a soybean class are significantly underestimated. These gross discrepancies can be alleviated to some extent if land classification information is available on subpixel scales that can be used to reliably compute the fraction of corn and soybean within each coarse-scale cell. The utility of this subpixel information is demonstrated in Fig. 10 ("mixed class" panels); the aggregation is improved in comparison with method A, yet still not scale invariant. At the 5-km scale, the residual bias is 0.5 kg m^{-2} for θ_{veg} and 0.14 m for h_c, comparable to the RMSD values associated with the high-resolution retrievals themselves.

These results support work by DeFries et al. (1997), who aggregated biophysical parameters from the 8-km scale to the 1×1 deg (110×110 km at equator) and 4×5 deg scales typical of many continental and global modeling schemes. They found that inclusion of subpixel classification information improved the accuracy of roughness estimates (dependent on canopy height), but that improvements were modest over these scales. Fig. 10 suggests the benefits may be more significant on smaller scales, closer to the nominal patch size.

5. Conclusions

Vegetation indices derived from multispectral reflectance data collected at 1.5-m resolution by aircraft and at 30-m

Table A1
Field-scale mean and standard deviation (in italics) in LAI, vegetation water content, and canopy height for each SMEX02 watershed-sampling site, computed within field bounding boxes shown in Fig. 1 from retrievals based on $OSAVI_{USU}$, $OSAVI_{TM}$, and $NDWI_{TM}$ data sets

	Leaf area index (m^2/m^2)								Vegetation water content (kg/m^2)								Canopy height (m)							
	16 June $OSAVI_{USU}$		23 June $OSAVI_{TM}$		1 July $NDWI_{TM}$		8 July $NDWI_{TM}$		16 June $OSAVI_{USU}$		23 June $OSAVI_{TM}$		1 July $NDWI_{TM}$		8 July $NDWI_{TM}$		16 June $OSAVI_{USU}$		23 June $OSAVI_{TM}$		1 July $NDWI_{TM}$		8 July $NDWI_{TM}$	
WC01	-unavailable[a]-		1.83	*0.21*	3.19	*0.40*	4.20	*0.35*	unavailable[a]		1.69	*0.22*	3.05	*0.47*	4.41	*0.47*	unavailable[a]		0.99	*0.08*	1.31	*0.14*	1.69	*0.13*
WC03	0.40	*0.10*	0.84	*0.21*	1.63	*0.20*	2.76	*0.19*	0.12	*0.02*	0.24	*0.06*	0.47	*0.06*	0.79	*0.06*	0.15	*0.01*	0.21	*0.03*	0.31	*0.02*	0.42	*0.02*
WC04	0.98	*2.17*	2.04	*0.36*	3.64	*0.40*	4.63	*0.32*	0.85	*0.20*	1.92	*0.39*	3.64	*0.51*	5.02	*0.46*	0.63	*0.10*	1.06	*0.13*	1.48	*0.15*	1.86	*0.13*
WC05	1.18	*0.16*	2.05	*0.17*	3.42	*0.29*	4.27	*0.31*	1.03	*0.14*	1.92	*0.19*	3.34	*0.36*	4.50	*0.42*	0.72	*0.07*	1.07	*0.06*	1.40	*0.10*	1.72	*0.12*
WC06	1.07	*0.21*	2.33	*0.39*	3.69	*0.49*	4.64	*0.56*	0.93	*0.19*	2.24	*0.43*	3.72	*0.62*	5.05	*0.76*	0.67	*0.09*	1.16	*0.13*	1.50	*0.18*	1.87	*0.21*
WC08	0.99	*0.18*	1.94	*0.24*	3.50	*0.25*	4.37	*0.26*	0.85	*0.16*	1.80	*0.26*	3.44	*0.33*	4.64	*0.37*	0.63	*0.08*	1.03	*0.09*	1.43	*0.09*	1.76	*0.10*
WC09	0.56	*0.20*	1.20	*0.20*	1.83	*0.18*	2.89	*0.22*	0.16	*0.06*	0.35	*0.07*	0.52	*0.05*	0.83	*0.06*	0.17	*0.03*	0.25	*0.03*	0.33	*0.02*	0.43	*0.02*
WC10	0.64	*0.15*	1.18	*0.13*	1.99	*0.18*	2.91	*0.30*	0.18	*0.04*	0.34	*0.04*	0.57	*0.05*	0.83	*0.09*	0.18	*0.02*	0.25	*0.02*	0.35	*0.02*	0.43	*0.03*
WC11	1.10	*0.27*	2.03	*0.27*	3.44	*0.35*	4.33	*0.24*	0.96	*0.25*	1.91	*0.29*	3.37	*0.44*	4.58	*0.33*	0.68	*0.12*	1.06	*0.10*	1.41	*0.13*	1.74	*0.09*
WC12	0.95	*0.16*	1.83	*0.21*	3.14	*0.33*	4.09	*0.34*	0.82	*0.14*	1.69	*0.23*	2.99	*0.40*	4.25	*0.47*	0.61	*0.08*	0.99	*0.08*	1.30	*0.12*	1.65	*0.13*
WC13	0.23	*0.11*	0.69	*0.17*	1.28	*0.20*	2.01	*0.22*	0.07	*0.03*	0.19	*0.05*	0.37	*0.06*	0.57	*0.06*	0.12	*0.02*	0.19	*0.02*	0.26	*0.02*	0.35	*0.02*
WC14	0.72	*0.29*	1.22	*0.30*	1.97	*0.26*	2.96	*0.21*	0.20	*0.08*	0.35	*0.10*	0.56	*0.08*	0.85	*0.06*	0.19	*0.04*	0.26	*0.04*	0.35	*0.03*	0.44	*0.02*
WC15	1.07	*0.22*	2.06	*0.25*	3.45	*0.26*	4.50	*0.24*	0.93	*0.20*	1.94	*0.28*	3.38	*0.34*	4.83	*0.34*	0.67	*0.10*	1.07	*0.09*	1.41	*0.10*	1.81	*0.09*
WC16	0.63	*0.36*	1.24	*0.27*	1.87	*0.24*	2.85	*0.31*	0.18	*0.10*	0.36	*0.08*	0.53	*0.07*	0.82	*0.09*	0.18	*0.04*	0.26	*0.03*	0.34	*0.03*	0.43	*0.02*
WC17	0.86	*0.18*	1.97	*0.18*	3.58	*0.22*	4.75	*0.27*	0.74	*0.16*	1.84	*0.19*	3.55	*0.29*	5.20	*0.40*	0.57	*0.08*	1.04	*0.06*	1.46	*0.08*	1.91	*0.11*
WC18	1.06	*0.18*	2.13	*0.24*	3.60	*0.25*	4.40	*0.39*	0.92	*0.16*	2.02	*0.26*	3.58	*0.33*	4.70	*0.52*	0.67	*0.08*	1.10	*0.08*	1.47	*0.09*	1.77	*0.15*
WC19	1.12	*0.31*	1.95	*0.20*	3.34	*0.27*	4.14	*0.39*	0.98	*0.29*	1.82	*0.22*	3.24	*0.34*	4.33	*0.53*	0.69	*0.13*	1.03	*0.07*	1.37	*0.10*	1.67	*0.15*
WC20	1.32	*0.34*	2.25	*0.33*	3.45	*0.35*	4.38	*0.41*	1.17	*0.33*	2.15	*0.37*	3.39	*0.45*	4.67	*0.58*	0.78	*0.15*	1.13	*0.11*	1.41	*0.13*	1.77	*0.16*
WC21	0.45	*0.21*	1.01	*0.23*	1.54	*0.27*	2.22	*0.40*	0.13	*0.05*	0.29	*0.07*	0.44	*0.08*	0.64	*0.12*	0.15	*0.03*	0.23	*0.03*	0.30	*0.03*	0.37	*0.04*
WC22	0.13	*0.08*	0.37	*0.14*	1.09	*0.12*	1.74	*0.23*	0.05	*0.02*	0.11	*0.03*	0.31	*0.03*	0.50	*0.07*	0.11	*0.01*	0.14	*0.02*	0.24	*0.02*	0.32	*0.03*
WC23	0.34	*0.13*	0.84	*0.16*	1.78	*0.22*	2.76	*0.28*	0.10	*0.03*	0.24	*0.05*	0.51	*0.06*	0.79	*0.08*	0.14	*0.02*	0.21	*0.02*	0.33	*0.03*	0.42	*0.02*
WC24	1.23	*0.19*	2.18	*0.28*	3.73	*0.26*	4.62	*0.21*	1.08	*0.18*	2.07	*0.30*	3.75	*0.33*	5.01	*0.31*	0.74	*0.09*	1.11	*0.10*	1.51	*0.10*	1.86	*0.08*
WC25	1.02	*0.25*	1.34	*0.28*	2.26	*0.47*	2.83	*0.59*	0.88	*0.22*	1.19	*0.27*	1.99	*0.48*	2.64	*0.66*	0.64	*0.11*	0.79	*0.12*	0.98	*0.17*	1.19	*0.21*
WC26	1.01	*0.21*	1.84	*0.33*	3.53	*0.43*	4.43	*0.60*	0.88	*0.20*	1.71	*0.35*	3.50	*0.55*	4.75	*0.81*	0.64	*0.10*	0.99	*0.13*	1.44	*0.16*	1.79	*0.23*
WC27	0.45	*0.19*	1.03	*0.25*	2.25	*0.39*	3.48	*0.42*	0.39	*0.16*	0.90	*0.23*	1.97	*0.41*	3.43	*0.53*	0.38	*0.09*	0.65	*0.11*	0.98	*0.14*	1.42	*0.15*
WC28	1.19	*0.29*	2.15	*0.37*	3.74	*0.33*	4.72	*0.27*	1.04	*0.27*	2.04	*0.40*	3.77	*0.44*	5.16	*0.40*	0.72	*0.13*	1.10	*0.13*	1.52	*0.12*	1.90	*0.11*
WC29	1.25	*0.29*	1.98	*0.40*	3.93	*0.56*	5.01	*0.52*	1.10	*0.27*	1.86	*0.43*	4.05	*0.73*	5.60	*0.76*	0.75	*0.13*	1.04	*0.15*	1.59	*0.21*	2.02	*0.21*
WC30	1.19	*0.29*	1.95	*0.36*	3.69	*0.35*	4.67	*0.32*	1.04	*0.28*	1.83	*0.38*	3.71	*0.45*	5.09	*0.46*	0.72	*0.13*	1.03	*0.13*	1.50	*0.13*	1.88	*0.13*
WC31	1.45	*0.18*	2.22	*0.28*	4.14	*0.37*	5.23	*0.51*	1.29	*0.18*	2.12	*0.31*	4.33	*0.50*	5.94	*0.75*	0.84	*0.08*	1.13	*0.10*	1.67	*0.14*	2.11	*0.20*
WC32	0.37	*0.15*	0.90	*0.18*	1.56	*0.18*	2.31	*0.26*	0.11	*0.04*	0.25	*0.05*	0.44	*0.05*	0.66	*0.08*	0.14	*0.02*	0.21	*0.02*	0.30	*0.02*	0.38	*0.03*
WC33	0.76	*0.19*	1.59	*0.21*	3.06	*0.32*	4.13	*0.31*	0.65	*0.17*	1.44	*0.21*	2.90	*0.38*	4.30	*0.43*	0.53	*0.09*	0.90	*0.09*	1.27	*0.11*	1.67	*0.12*

[a] USU aircraft imagery did not include WC01.

resolution by Landsat over the Walnut Creek Watershed during the SMEX02/SMACEX experiments were used to develop regression equations with respect to an extensive set of ground-based measurements of leaf area index, vegetation water content, and canopy height. The remote sensing data provide means for spatially weighting in-field variability in upscaling the ground data to field scale and larger scales. They also allow estimation of canopy conditions in fields in the study area that were not sampled. At the observation scale (~10 m), retrieval accuracy is 15–20%, with root-mean-square deviations of 0.6 in LAI, 0.7 kg m^{-2} in vegetation water content, and 0.2 m in canopy height.

Given the patchwork spatial structure characteristic of the central Iowa landscape, it was demonstrated that the process of aggregating canopy conditions up to field scales was independent of the resolution of the remote sensing data used provided that individual fields are well resolved by the imagery, eliminating pixels of mixed land-cover types. This indicates that the variability between canopy properties and vegetation indices that exist within fields is largely linear. Variability between fields can be strongly nonlinear, particularly for canopy height and vegetation water; thus, imagery at resolutions coarser than field scale (~500 m) will yield poor aggregate values unless subpixel information about cropping fractions is available. The transformation from reflectance to NDWI in this landscape, however, is effectively scale invariant over scales from 30 m to 5 km.

The NDVI and OSAVI indices suffer saturation over cornfields near the end of SMEX02 when LAI exceeds 3–3.5, degrading spatial averages and amplifying variability in biophysical properties retrieved using these indices. Soybean is not affected by saturation during SMEX02. The Landsat TM includes a SWIR band used in the NDWI index, which has greater sensitivity to vegetation water content and does not saturate over the course of the experiment, extending the retrieval saturation limit to LAI>4. Of the indices studied, NDWI is therefore preferable for upscaling ground-based canopy measurements made during the latter half of SMEX02. Maps of biophysical properties retrieved from meter-scale-resolution imagery collected by aircraft will be valuable for detailed in-field studies of soil moisture variability and simulations of land-atmosphere coupling.

Acknowledgements

Funds provided by USDA-ARS Cooperative Agreement 58-1265-1-0043 helped to support field measurement and analysis activities related to SMEX02/SMACEX. The SMACEX project was made possible by funding provided by NASA grant S-44825-G under NRA 00-OES-07 from the NASA Terrestrial Hydrology Program. Logistical support from the USDA-ARS National Soil Tilth Lab was critical to the success of both field campaigns. Special thanks are extended to all of the volunteers who participated in vegetation data collection during SMEX02.

Appendix A

For the benefit of scientists working with data collected during the SMEX02 and SMACEX experiments, best estimates of field-scale mean canopy properties and in-field variability for four days during SMEX02, at each of the sampling sites in the Walnut Creek Watershed, are tabulated in Table A1. These spatial statistics have been retrieved from the full-resolution aircraft and Landsat remote sensing data sets as described in the main text. Retrievals using the OSAVI index are reported for June 16 and 23, when the scene contained partial ground cover. For July 1 and 8, when OSAVI is showing signs of saturation, NDWI-based aggregate values are given.

References

Berk, A., Bernstein, L. S., Anderson, G. P., Acharya, P. K., Robertson, D. C., Chetwynd, J. H., et al. (1998). MODTRAN cloud and multiple scattering upgrades with application to AVIRIS. *Remote Sensing of Environment*, *65*, 367–375.

Cai, B., & Neale, C. M. U. (1999). A method for constructing 3-dimensional models from airborne imagery. *Color Photography and Videography for Resource Assessment. Proceedings of the 17th Biennial Workshop* (pp. 231–246). Bethesda, MD: American Society for Photogrammetry and Remote Sensing.

Carlson, T. N., Perry, E. M., & Schmugge, T. J. (1990). Remote estimation of soil moisture availability and fractional vegetation cover for agricultural fields. *Agricultural and Forest Meteorology*, *52*, 45–69.

De Cola, L. (1997). Multiresolution covariation among Landsat and AVHRR vegetation indices. In D. A. Quattrochi, & M. F. Goodchild (Eds.), *Scale in remote sensing and GIS* (pp. 73–91). Boca Raton, FL: CRC Lewis.

DeFries, R. S., Townshend, J. R., & Los, S. O. (1997). Scaling land cover heterogeneity for global atmosphere–biosphere models. In D. A. Quattrochi, & M. F. Goodchild (Eds.), *Scale in remote sensing and GIS* (pp. 231–246). Boca Raton: CRC Lewis.

Doraiswamy, P. C., Hatfield, J. L., Jackson, T. J., Akhmedoc, B., Prueger, J., & Stern, A. (2004). Crop condition and yield simulations using Landsat and MODIS. *Remote Sensing of Environment*, 92, 548-559. doi:10.1016/j.rse.2004.05.017.

Eichinger, W. E., Cooper, D. I., Hipps, L. E., Kustas, W. P., Neale, C. M. U., & Prueger, J. H. (2003). High resolution lidar evaporative fluxes over corn and soybean crops in Central Iowa during SMACEX. *17th Conference on Hydrology*. Long Beach, CA: American Meteorological Society.

Friedl, M. A., Davis, F. W., Michaelsen, J., & Moritz, M. A. (1995). Scaling and uncertainty in the relationship between NDVI and land surface biophysical variables: An analysis using a scene simulation model and data from FIFE. *Remote Sensing of Environment*, *54*, 233–246.

Gao, B. (1996). NDWI—A normalized difference water index for remote sensing of vegetation liquid water from space. *Remote Sensing of Environment*, *58*, 257–266.

Gitelson, A. A., Viña, A., Arkebauer, T. J., Rundquist, D. C., Keydan, G., & Leavitt, B. (2003). Remote estimation of leaf area index and green leaf biomass in maize canopies. *Geophysical Research Letters*, *30*. doi:10.1029/2002GL016450.

Gobron, N., Pinty, B., & Verstraete, M. M. (1997). Theoretical limits to the estimation of the leaf area index on the basis of visible and near-infrared remote sensing data. *IEEE Transactions on Geoscience and Remote Sensing*, *35*, 1438–1445.

Hall, F. G., Huemmrich, K. F., Goetz, S. J., Sellers, P. J., & Nickerson, J. E. (1992). Satellite remote sensing of surface energy balance: Success,

failures and unresolved issues in FIFE. *Journal of Geophysical Research*, *97*, 19061–19089.

Hardisky, M. A., Lemas, V., & Smart, R. M. (1983). The influence of soil salinity, growth form, and leaf moisture on the spectral reflectance of *Spartina alternifolia* canopies. *Photogrammetric Engineering and Remote Sensing*, *49*, 77–83.

Huete, A. R. (1988). A soil-adjusted vegetation index (SAVI). *Remote Sensing of Environment*, *27*, 47–57.

Jackson, T. J., Chen, D., Cosh, M. H., Li, F., Anderson, M. C., Walthall, C., et al. (2004). Vegetation water content mapping using Landsat TM derived NDWI for corn and soybean. *Remote Sensing of Environment.*

Jackson, T. J., & O'Neill, P. E. (1990). Attenuation of soil microwave emission by corn and soybeans at 1.4 and 5 GHz. *IEEE Transactions on Geoscience and Remote Sensing*, *28*, 978–980.

Jackson, T. J., & Schmugge, T. J. (1991). Vegetation effects on the microwave emission of soils. *Remote Sensing of Environment*, *36*, 203–212.

Kriegler, F. J., Malila, W. A., Nalepka, R. F., & Richardson, W. (1969). Preprocessing transformations and their effects on multispectral recognition. *Sixth International Symposium on Remotes Sensing of Environment, Ann Arbor, MI* (pp. 97–131).

Li, F., Jackson, T. J., Kustas, W. P., Schmugge, T. J., French, A. N., Cosh, M., & Bindlish, R. (2004). Deriving land surface temperature from Landsat 5 and 7 during SMEX02/SMACEX. *Remote Sensing of Environment.*

Neale, C. M. U., & Crowther, B. G. (1994). An airborne multispectral video/radiometer remote sensing system: Development and calibration. *Remote Sensing of Environment*, *48*, 1–25.

Quattrochi, D. A., & Goodchild, M. F. (Eds.) (1997). *Scale in remote sensing* (pp. 309–317). Boca Raton: CRC Lewis. 406 pp.

Rondeaux, G., Steven, M., & Baret, F. (1996). Optimisation of soil-adjusted vegetation indices. *Remote Sensing of Environment*, *55*, 95–107.

Rouse, J. W., Haas, R. H., Schell, J. A., & Deering, D. W. (1973). Monitoring vegetation systems in the Great Plains with ETRS. *Third ETRS Symposium, NASA SP353, Washington DC* (pp. 309–317).

Sellers, P. J. (1987). Canopy reflectance, photosynthesis, and transpiration: II. The role of biophysics in the linearity of their interdependence. *Remote Sensing of Environment*, *21*, 143–183.

Thenkabail, P. S., Ward, A. D., Lyon, J. G., & Merry, C. J. (1994). Thematic Mapper vegetation indices for determining soybean and corn growth parameters. *Photogrammetric Engineering and Remote Sensing*, *60*, 437–442.

Tucker, C. J., Elgin, J. H., McMurtrey III, J. E., & Fan, C. J. (1979). Monitoring corn and soybean crop development with hand-held radiometer spectral data. *Remote Sensing of Environment*, *8*, 237–248.

Vermote, E., Tanré, D., Deuzé, J. L., Herman, M., & Morcette, J. J. (1997). Second simulation of the satellite signal in the solar spectrum: An overview. *IEEE Transactions on Geoscience and Remote Sensing*, *35*, 675–686.

Verstraete, M. M., Pinty, B., & Myneni, R. B. (1996). Potential limitations of information extraction on the terrestrial biosphere from satellite remote sensing. *Remote Sensing of Environment*, *58*, 201–214.

Vogelmann, J. E., & DeFelice, T. P. (2003). Characterization of intra-annual reflectance properties of land cover classes in southeastern South Dakota using Landsat Tm and ETM+ data. *Canadian Journal of Remote Sensing*, *29*, 219–229.

Welles, J. M., & Norman, J. M. (1991). Instrument for indirect measurement of canopy architecture. *Agron. J.*, *83*, 818–825.